On the efficiency of 1D atom localisation via EIT in a degenerate two-level atomic system

Jelena Dimitrijević, Dušan Arsenović and Branislav M Jelenković

Institute of Physics, University of Belgrade, Pregrevica 118 11080 Belgrade

E-mail: jelenad@ipb.ac.rs

Abstract

We analyse one-dimensional (1D) subwavelength atom localisation in a cold atomic medium under the action of two optical fields, the standing-wave and travelling probe fields, in the presence of a magnetic field. Optical Bloch equations are solved numerically for the hyperfine atomic transition $F_g = 2 \rightarrow F_e = 1$ of the ^{87}Rb D1 line. All Zeeman sublevels are included in the calculations. This atomic scheme allows electromagnetically induced transparency (EIT) if the applied magnetic field is zero or small. The results for the position-dependent probe absorption are presented for two configurations, depending on the orientation of the magnetic field with respect to the optical fields' polarisations. The efficiency of the atom localisation is analysed for a large range of field intensities and applied magnetic fields. The observed behaviour of the probe absorption is analysed through the effects of EIT induced by two fields of various strengths and its dependence on the applied magnetic fields.

Keywords: 1D atom localisation, electromagnetically induced transparency, Zeeman effect

(Some figures may appear in colour only in the online journal)

1. Introduction

During the past two decades there has been considerable attention in developing various techniques for precision position measurements of an atom moving through a standing-wave field [1]. Due to the fact that the dynamics of the atomic systems is position dependent within a standing-wave, by measuring the position-dependent quantities of the system, one can attain information on the position of the atom in the subwavelength domain. Interest in studying the atom localisation effect lies in potential applications for the precise measurement of atom position in laser cooling and trapping of atoms [2, 3], Bose–Einstein condensation [4, 5], atom nanolithography [6–8], the measurement of the centre-of-mass wave function of moving atoms [9, 10] etc.

Early developed methods for atom localisation were based on measurements of the phase shifts of standing waves [11, 12], or atomic dipole [13, 14], resonance imaging methods [15, 16] entanglement between the atom position and its internal state [17], Ramsey interferometry [18] etc. Recent techniques to achieve atom localisation are mainly based on the atomic coherence of internal states and quantum-interference effects.

Considerable interest is in realising atom localisation by coherent population trapping [19] and electromagnetically induced transparency (EIT) [20], also phase-dependent EIT in closed-loop atomic schemes, Autler–Townes microscopy [21], STIRAP (stimulated Raman adiabatic passage) [22] etc. Studies were performed by utilising position-dependent quantities like probe field absorption [23, 24], atom excited state population [25–27], spontaneously emitted photon [21, 28–31] and Raman gain [32, 33].

While early studies on atom localisation were mainly for one-dimensional localisation, recent studies also analyse realisations of two-dimensional localisation [24, 30, 31], since they provide more information on the atom position, better spatial resolution and could potentially find more applications. Moreover, recent studies [34, 35] suggest the realisation of three-dimensional atom localisation. The newly established domain of subwavelength localisation, named sub-half-wavelength localisation, analyses techniques that give information on the atom position within the half wavelength distance [29, 36, 37]. Only a few experimental realisations of the atom localisation effect have been performed [34, 38–40] so far.

In studies of atom localisation, an atom is considered to be localised if narrow structures can be observed in the

localisation pattern, i.e. a position dependence of measurable quantity. The number of narrow structures in one sub-wavelength domain shows the detecting probability, the width shows the localisation precision, while the positions indicate where the atom is localised. Most theoretical studies on atom localisation use simple atomic schemes constituted of several atomic levels. This enables analytical expressions to be obtained from which one can read the choice of parameters (field strengths, detunings, relative phase etc) which yields the most efficient atom localisation.

We perform a numerical study and analyse the efficiency of one-dimensional (1D) atom localisation by using two orthogonal optical fields, the standing-wave and travelling probe fields. Atom localisation studies often use the detuning of the optical field from the resonance for control of localisation. Here, we assume that both fields are on the resonance of $F_g = 2 \rightarrow F_e = 1$ transition, D1 line in ^{87}Rb, while the shift of energy levels from the resonances is done by applying a magnetic field. This atomic scheme is known to support Zeeman EIT, a quantum phenomenon due to the coherent superposition of magnetic sublevels, manifested in the reduced absorption of the optical field if zero or a small magnetic field is applied. The numerical calculations are done by solving Optical Bloch equations for a multiple-level atomic scheme with all the Zeeman sublevels taken into consideration. Two configurations, with different orientations of magnetic field, along the standing-wave or along the probe field polarisation, are analysed. The advantage of numerical analysis is that we can apply arbitrary strengths of optical and magnetic fields. The optical fields' intensities range from 10^{-4} to 10^2 mW cm^{-2}, the while magnetic fields range from 0 to 5 *G*. We analyse the behaviour of the localisation patterns obtained from the probe field absorption, investigating the effects of standing-wave and probe intensities, and also the influence of magnetic fields on the efficiency of 1D atom localisation.

2. 1D atom localisation schemes and theoretical model

We analyse a scheme with two optical fields, standing-wave and travelling probe fields interacting with cold atoms, in the presence of a magnetic field. Both fields are linearly polarised with mutually orthogonal polarisations and propagation directions. We analyse two configurations, i.e. the directions of the standing-wave and probe field polarisation with respect to the applied magnetic field:

- Configuration **A**: The optical standing-wave is linearly polarised along the magnetic field direction and aligned along the *y*-direction. The probe field is linearly polarised in the *y*-direction and propagates along the *z*-axis (see figure 1(a)).
- Configuration **B**: The probe field electric vector is collinear with the magnetic field, while the standing-wave is polarised in the *y*-direction and aligned along the *x*-axis (see figure 1(b)).

Steady-state optical Bloch equations (OBE) are solved for the $F_g = 2 \rightarrow F_e = 1$ transition (see figure 2) in ^{87}Rb, D1 line,
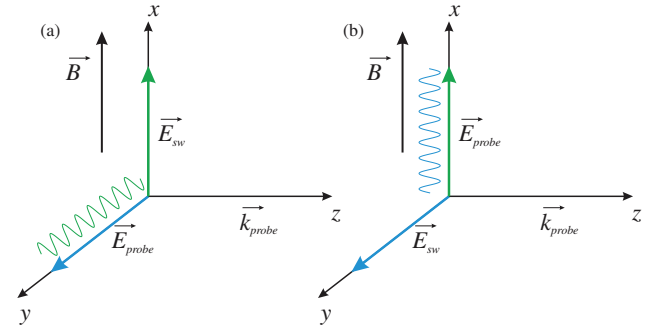

Figure 1. The geometry of the experiment, with applied magnetic field $\vec{B}$ and two linearly polarised, mutually orthogonal optical fields, standing-wave and probe fields with electric vectors $\vec{E}_{sw}(\vec{r}, t)$ and $\vec{E}_{probe}(\vec{r}, t)$. $\vec{k}_{probe}$ is the probe field wave-vector. (a) shows the configuration **A**: $\vec{E}_{sw} \| \vec{B} \perp \vec{E}_{probe}$; (b) is the scheme for configuration **B**: $\vec{E}_{probe} \| \vec{B} \perp \vec{E}_{sw}$, where we omit the dependence on t and $\vec{r}$.
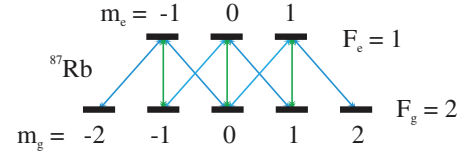

Figure 2. $F_g = 2$ and $F_e = 1$ hyperfine levels, with notation of magnetic sublevels and dipole allowed transitions due to selection rules $\Delta m = 0$ (green lines) and $\Delta m = \pm 1$ (blue lines).

for different applied magnetic fields and magnitudes of optical fields' intensities. From OBE:

$$\frac{i}{\hbar}[\hat{H}_0, \hat{\rho}] + \frac{i}{\hbar}[\hat{H}_I, \hat{\rho}] - \hat{S}E\hat{\rho} + \gamma\hat{\rho} = \gamma\hat{\rho}_0, \quad (1)$$

we calculate the elements of density matrix $\hat{\rho}$. The diagonal elements of the density matrix, ρ_{g_i, g_i} and ρ_{e_i, e_i} are the populations, the elements ρ_{g_i, g_j} and ρ_{e_i, e_j} are the Zeeman coherences, and ρ_{g_i, e_j} and ρ_{e_i, g_j} are the optical coherences. Here, indexes *g* and *e* stand for the ground and the excited levels, respectively.

In equation (1), $\hat{H}_0$ is a Hamiltonian describing Rb atoms in magnetic field $\vec{B}$:

$$\hat{H}_0 = \sum_{i=1}^{2F_g+1} \hbar\omega_{g_i}|g_i\rangle\langle g_i| + \sum_{i=1}^{2F_e+1} \hbar\omega_{e_i}|e_i\rangle\langle e_i|. \quad (2)$$

The magnetic sublevels are split due to the Zeeman effect by $\mathcal{E}_{g_i} = \hbar\omega_{g_i} = \mathcal{E}_{F_g=2} + \mu_B l_{F_g} m_{g_i} B$ for ground-state sublevels and $\mathcal{E}_{e_i} = \hbar\omega_{e_i} = \mathcal{E}_{F_e=1} + \mu_B l_{F_e} m_{e_i} B$ for excited, where $m_{g(e)}$ are the magnetic quantum numbers of the ground and excited levels, μ_B is the Bohr magneton and $l_{F_{g(e)}}$ are Lande the gyromagnetic factors for the hyperfine levels. $\mathcal{E}_{F_g=2}$ and $\mathcal{E}_{F_e=1}$ are the energies of hyperfine levels $F_g = 2$ and $F_e = 1$ of the free atom, respectively.

The interaction of atoms with two optical fields is given with the Hamiltonian:

$$\hat{H}_I = -\hat{\vec{d}} \cdot \vec{E}(\vec{r}, t) = \sum_{i=1}^{2F_g+1}\sum_{j=1}^{2F_e+1} V_{g_i, e_j}|g_i\rangle\langle e_j| + \text{h.c.}, \quad (3)$$
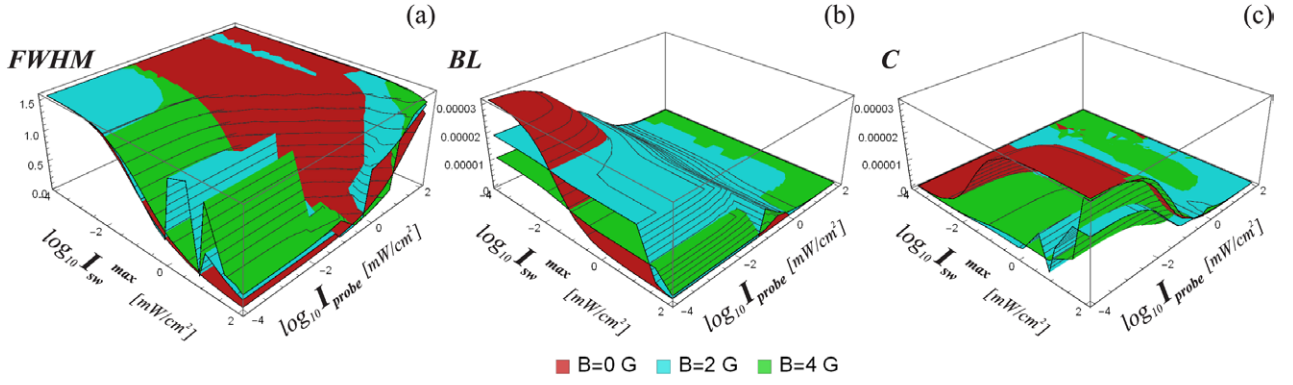
Figure 3. Results for configuration **A**: three-dimensional representation of the FWHM (a), base-level (b) and contrast (c) of the localisation pattern structures obtained from the probe absorption A_{probe} dependence on the normalised position $k_{sw}y$. The magnitudes of both optical field intensities take values from 10^{-4} to 10^2 mW cm^{-2} and are given on the logarithmic scale. Several surfaces correspond to several values of the magnetic field $B = 0$, 2 and 4 G.

where $\hat{\vec{d}}$ is the electric dipole operator and $\vec{E}(\vec{r}, t)$ is the total electric field oscillating with angular frequency $\omega_l = \frac{\mathcal{E}_{F_e=1} - \mathcal{E}_{F_g=2}}{\hbar}$, i.e. both fields are on the resonance of $F_g = 2 \rightarrow F_e = 1$ transition, the D1 line in ^{87}Rb. V_{g_i, e_j} are the matrix elements of the electric dipole interaction. $\hat{SE}$ stands for the spontaneous emission operator with rate Γ. We assume relaxation of all the density matrix elements with small rate $\gamma \ll \Gamma$ due to the mechanism like the finite time of flight or collisional decay [41]. The term $\gamma \hat{\rho}_0$ describes the repopulation of the atomic sample at the same rate, where ρ_0 describes atoms in their initial state, equal population of the ground Zeeman sublevels. As we are considering cold atomic sample, the role of Doppler broadening is not discussed.

We apply a Raman–Nath approximation [42], i.e. the centre-of-mass position of an atom along the direction of the standing-wave field is nearly constant and therefore we neglect the atom's kinetic energy in the Hamiltonian. An electric dipole and rotating-wave approximations were applied. The quantisation axis is taken along magnetic field vector $\vec{B}$, and equations (1) are solved in the rotated coordinate system for all Zeeman sublevels of the $F_g = 2$ and $F_e = 1$ hyperfine levels.

With the quantisation axis along magnetic field vector, two configurations allow different dipole-allowed transitions between the Zeeman magnetic sublevels in the considered atomic scheme (see figure 2 and the indicated different colours). For the first configuration **A**, the standing-wave field is π-polarised and $\Delta m = 0$ transitions are allowed, while the linearly polarised probe field introduces multiple Λ-schemes with σ^+ and σ^- light components of equal strength. Conversely, for the configuration **B**, for the probe field the selection rule $\Delta m = 0$ stands, while for the standing-wave field the selection rules are $\Delta m = \pm 1$.

We calculate the probe absorption coefficient A_{probe} as an imaginary part of the complex susceptibility tensor diagonal elements. For the configuration **A**, with the probe field along the y-axis, the probe absorption is calculated from:

$$A_{probe} = \text{Im}(\chi_{probe}) = \text{Im}[\frac{ieRN_c}{6\sqrt{2}\,\varepsilon_0 E_{probe}}(3\sqrt{2}\,\rho_{g_{-2}, e_{-1}} + 3\rho_{g_{-1}, e_0}$$
$$+ \sqrt{3}\,\rho_{g_0, e_{-1}} + \sqrt{3}\,\rho_{g_0, e_1} + 3\rho_{g_1, e_0} + 3\sqrt{2}\,\rho_{g_2, e_1})] \quad (4)$$

and for the configuration **B** and $\vec{E}_{probe}$ along the x-axis is given as:

$$A_{probe} = \text{Im}(\chi_{probe}) = \text{Im}[\frac{eRN_c}{6\varepsilon_0 E_{probe}}$$
$$\times (3\rho_{e_{-1}, g_{-1}} + 2\sqrt{3}\,\rho_{e_0, g_0} + 3\rho_{e_1, g_1})], \quad (5)$$

where N_c is the atom concentration, e is the elementary charge, ε_0 is the permittivity of the vacuum and $R = <J_g\|\vec{r}\|J_e>$ is the transition dipole matrix element.

3. Results and discussion

We calculate the localisation patterns, that is, the probe absorption versus the normalised positions ($k_{sw}x$ or $k_{sw}y$) within the standing-wave range $\{-\frac{\lambda}{2}, \frac{\lambda}{2}\}$. To calculate the localisation structures we use the same values of parameters for both configurations: the concentration of Rb atoms in the sample is $N_c = 10^{16}\,\frac{1}{m^3}$, the relaxation rate is $\gamma = 0.001\,\Gamma$ and the spontaneous emission rate is $\Gamma = 2\pi 5.750\,06$ MHz. The results are analysed for the range of applied standing-wave and probe field intensities (I_{sw} and I_{probe}, respectively) from 10^{-4} to 10^2 mW cm^{-2}. We vary the magnetic field between 0 and 5 G, staying in the vicinity of the EIT resonance.

Besides obtaining narrow structures in the localisation pattern, important for an experimental realisation of atom localisation is the ability to resolve the absorption levels in the localisation pattern. Therefore, we analysed the behaviour of the base-level, contrast and also full width at half maximum (FWHM) of the narrow peaks shown in the localisation patterns. In order to determine the structures in the localisation pattern, we calculated extrema of the A_{probe} versus $k_{sw}x$ (or $k_{sw}y$) curve. The structure is defined by one of these extrema, as its middle point, and its two adjacent extrema. The base-level represents the minimal absorption of the structure and the contrast is taken between the central and border extrema, where we take the smaller value if the peak is asymmetric. The FWHM is calculated as the width of the peak at half of the contrast height.
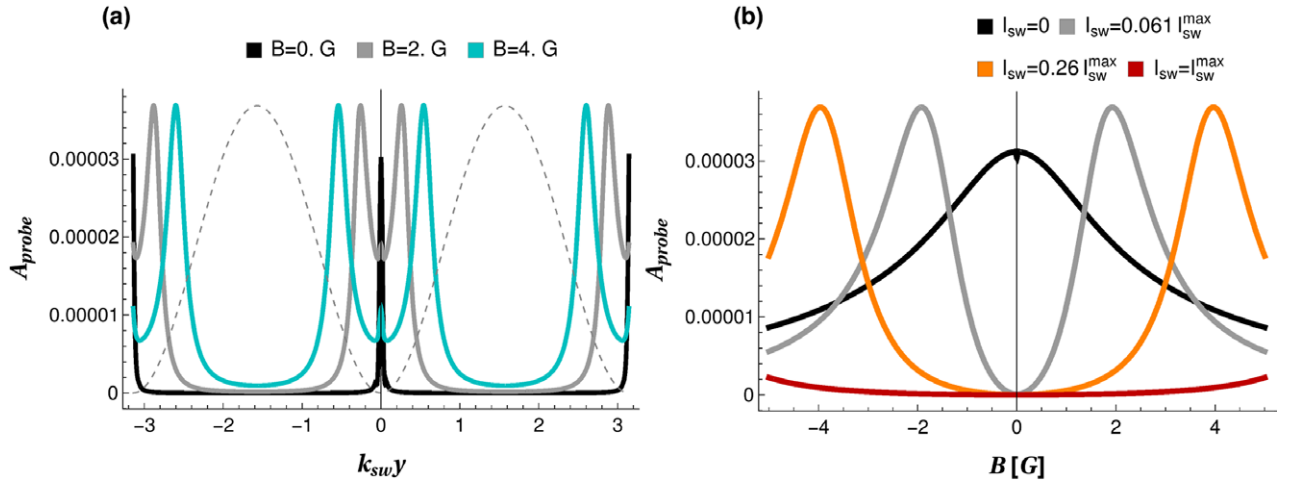
(a)

(b)

Figure 4. Configuration A: A_{probe} versus $k_{\text{sw}}y$ (a) and A_{probe} versus B (b) for fields' intensities $I_{\text{sw}}^{\text{max}} = 100$ mW cm^{-2} and $I_{\text{probe}} = 10^{-3}$ mW cm^{-2}. The results in (a) are for magnetic fields $B = 0$, 2 and 4 G and in (b) for standing-wave intensities $I_{\text{sw}} = 0$, 0.061, 0.26 and 1 $I_{\text{sw}}^{\text{max}}$. The dashed line in (a) shows normalised standing-wave intensity $I_{\text{sw}} = I_{\text{sw}}^{\text{max}} \sin^2(k_{\text{sw}}y)$. The curves in (b) for $I_{\text{sw}} = $ 0.061 and 0.26 $I_{\text{sw}}^{\text{max}}$ correspond to the positions of four peaks in (a) for B = 2 and 4 G, respectively.

3.1. Configuration A

In configuration **A**, as shown in figure 1(a), standing-wave electric vector $\vec{E}_{\text{sw}}$ is parallel to the magnetic field $\vec{B}$. In figure 3 we present the results for the FWHM (a), base-level (b) and contrast (c) of the localisation pattern structures for intensities, I_{probe} and $I_{\text{sw}}^{\text{max}}$, from 10^{-4} to 10^2 mW cm^{-2} given on the logarithmic scale. The results presented here are for three values of the magnetic field, $B = 0$, 2 and 4 G, while our analysis includes more values. The results for the widths of the structures show that, for $I_{\text{sw}}^{\text{max}} < 10^{-2}$ mW cm^{-2}, information on the atom position is available in a very broad region, i.e. the localisation structures have FWHM $\approx \frac{\lambda}{4}$, which indicates poor localisation precision. With the increase in $I_{\text{sw}}^{\text{max}}$ the widths reduce and for $I_{\text{probe}} < 1$ mW cm^{-2} extremely narrow structures can be obtained. The base level of the structures strongly depends on the probe field intensity and is low for $I_{\text{probe}} > 1$ mW cm^{-2}. The contrast of the localisation structures is higher if $I_{\text{sw}}^{\text{max}}$ is large and I_{probe} is small. In the following, we present some results from the previously discussed range of intensities, which show efficient localisation and also the effects of the magnetic field on the atom localisation.

In figure 4 we present the results for the probe absorption versus normalised position (a) and versus magnetic field (b) for fields' intensities $I_{\text{sw}}^{\text{max}} = 100$ mW cm^{-2} and $I_{\text{probe}} = 10^{-3}$ mW cm^{-2}. The localisation pattern in figure 4(a) for $B = 0$ shows highly efficient localisation with two peaks within one wavelength of the standing-wave, at the nodes of the standing-wave. With the increase in the magnetic field, one peak at the node splits into two overlapped peaks, which reduces the detection probability by half. More importantly, the results for $B \neq 0$ show that for this range of intensities the magnetic field can be used to control the peak positions within the standing-wave, i.e. the increase in magnetic field uniformly shifts the positions of the four peaks from nodes towards the anti-nodes of the standing-wave.

The behaviour of the probe absorption within the standing-wave for different magnetic fields can be understood from the dependence of the Zeeman EIT profile on the applied standing-wave intensities. The results in figure 4(b) show the dependence of probe absorption on the magnetic field at several positions within the standing-wave. The splitting of the localisation peak for $B \neq 0$ (figure 4(a)) is due to two overlapping EIT profiles and higher values of the probe absorption away from the nodes, as shown in figure 4(b). The shift of the localisation peaks towards the anti-nodes, the with increase in magnetic field, can be attributed to EIT broadening. As depicted in figure 4(b), as $k_{\text{sw}}y$ approaches the anti-node, the amplitude of EIT remains nearly constant, while the width of EIT constantly increases with maximal absorption moving towards higher magnetic fields.

The effects of the stronger probe field are given in figure 5 for $I_{\text{sw}}^{\text{max}} = 100$ mW cm^{-2} and $I_{\text{probe}} = 0.5$ mW cm^{-2}. In figure 5(a) we present A_{probe} versus $k_{\text{sw}}y$ for magnetic fields $B = 0$, 0.04, 0.2 and 1.8 G. The presented results suggest ways to control the localisation peaks' contrast by small magnetic fields. The localisation peaks are at the nodes of the standing-wave and the peaks' height gradually increases by about five times as the magnetic field changes from $B = 0$ to $B = 0.2$ G. The observed increase in contrast is explained by the high-contrast of EIT for $I_{\text{sw}} = 0$ (shown in figure 5(b)). The contrast of the localisation peaks in figure 5(a) increases as long as the magnetic field is 'inside' the EIT transparency window ($B \leqslant 0.2$ G), i.e. the increase of B weakens EIT, which leads to higher absorption at the nodes of the standing-wave.

A further increase in the magnetic field leads to broadening of the localisation peaks in figure 5(a), while the result for $B = 1.8$ G shows the formation of a much narrower peak on top of the wider peak. The results in figure 5(b) for $I_{\text{sw}} > 0$ show a similar effect to the results in figure 4(b), i.e. the EIT amplitudes are at the same level and the width of the EIT peak
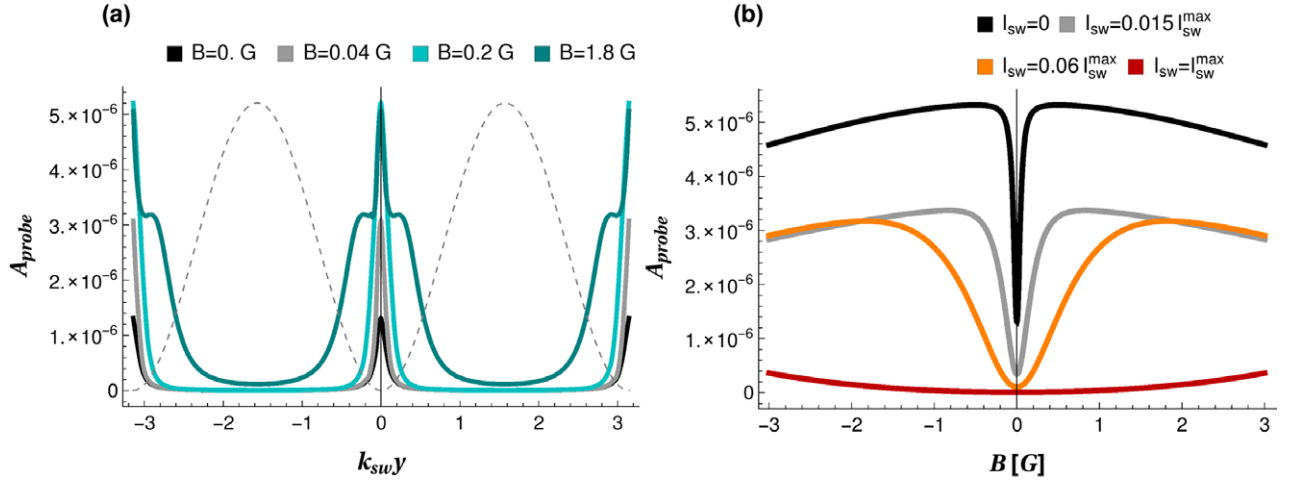
Figure 5. Configuration **A**: A_{probe} versus $k_{\mathrm{sw}}y$ (a) and A_{probe} versus B (b) for fields' intensities $I_{\mathrm{sw}}^{\mathrm{max}} = 100$ mW cm^{-2} and $I_{\mathrm{probe}} = 0.5$ mW cm^{-2}. The results in (a) are for magnetic fields $B = 0,\ 0.04,\ 0.2$ and 1.8 G and in (b) for standing-wave intensities $I_{\mathrm{sw}} = 0,\ 0.015,\ 0.06$ and $1\ I_{\mathrm{sw}}^{\mathrm{max}}$.
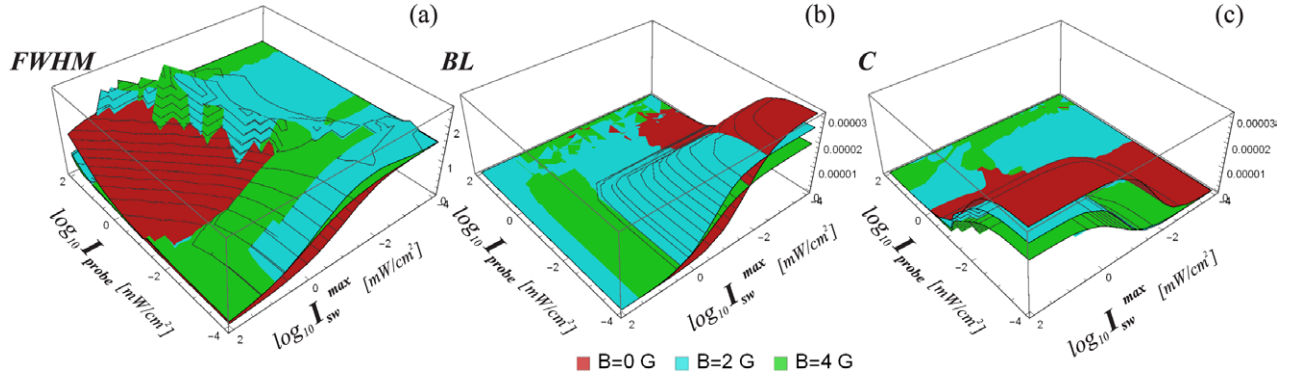

Figure 6. Results for configuration **B**: FWHM (a), base-level (b) and contrast (c) of the localisation patterns. The surfaces are drawn for 3 values of the magnetic fields $B = 0,\ 2$ and 4 G, while the maximal standing wave and probe field intensities are from 10^{-4} to 10^2 mW cm^{-2}.
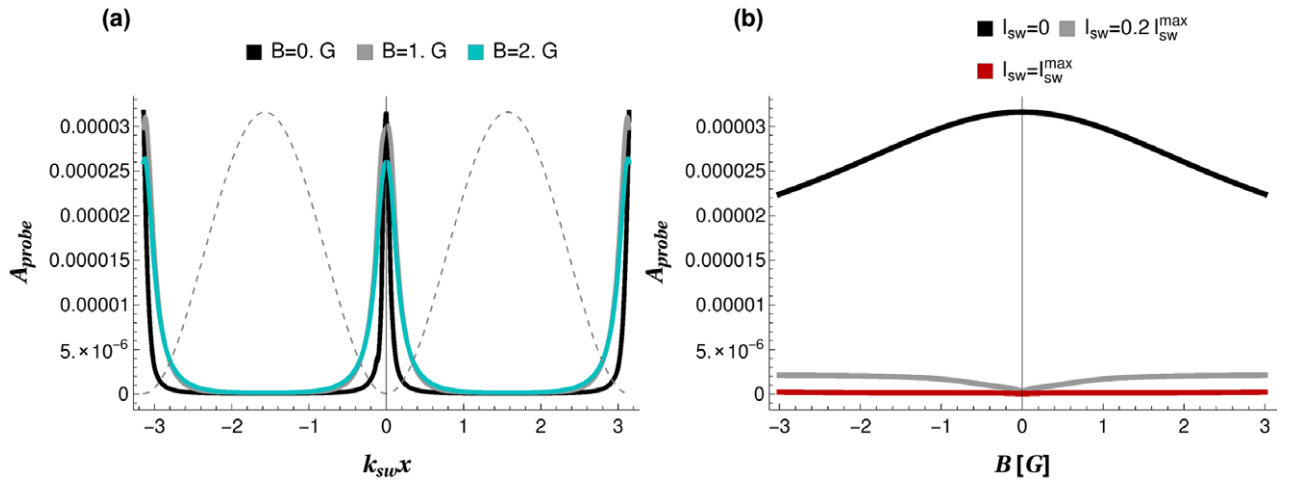

Figure 7. Configuration **B**: A_{probe} versus $k_{\mathrm{sw}}x$ (a) and A_{probe} versus B (b) for fields' intensities $I_{\mathrm{probe}} = 10^{-4}$ mW cm^{-2} and $I_{\mathrm{sw}}^{\mathrm{max}} = 10$ mW cm^{-2}. The results in (a) are for magnetic fields $B = 0,\ 1$ and 2 G and in (b) for standing-wave intensities $I_{\mathrm{sw}} = 0,\ 0.2$ and $1\ I_{\mathrm{sw}}^{\mathrm{max}}$. The dashed line in (a) shows the normalised standing-wave intensity $I_{\mathrm{sw}} = I_{\mathrm{sw}}^{\mathrm{max}} \sin^2(k_{\mathrm{sw}}x)$.

increases with the standing-wave intensity. For a small range of standing-wave intensities, the dependence of A_{probe} versus B shows overlapping for values of B outside of the EIT peaks indicating that the standing-wave intensity reached saturation intensity [43], i.e. a further increase in I_{sw} does not lead to higher one-photon absorption. The above explains the
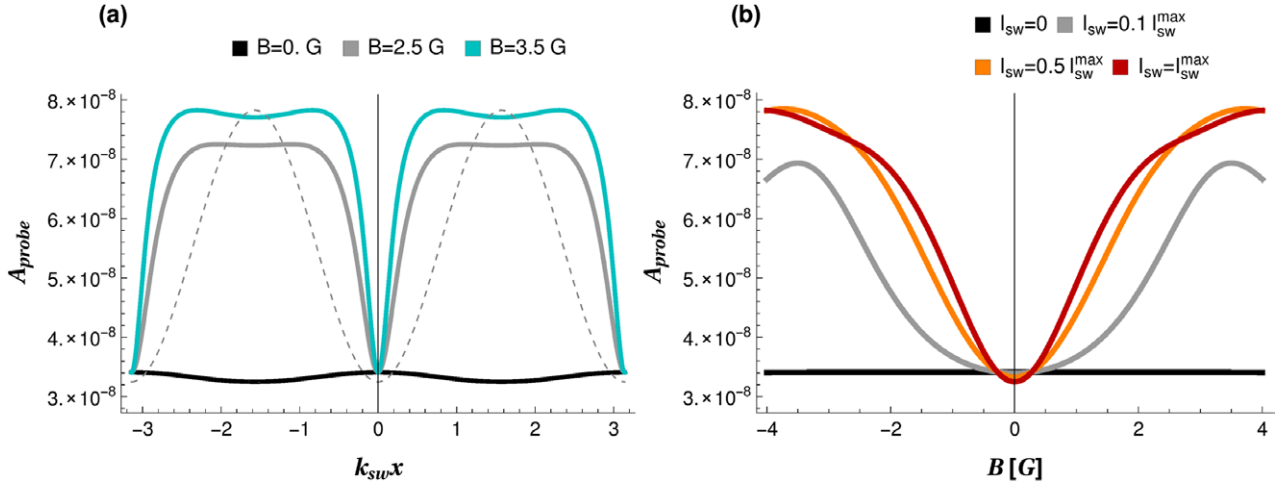
Figure 8. Configuration **B**: A_{probe} versus $k_{\text{sw}}x$ (a) and A_{probe} versus B (b) for fields' intensities $I_{\text{probe}} = 20$ mW cm^{-2} and $I_{\text{sw}}^{\text{max}} = 1$ mW cm^{-2}. The results in (a) are for magnetic fields $B = 0$, 2.5 and 3.5 G and in (b) for standing-wave intensities $I_{\text{sw}} = 0$, 0.1, 0.5 and 1 $I_{\text{sw}}^{\text{max}}$.

Figure 9. Configuration **B**: A_{probe} versus $k_{\text{sw}}x$ (a) and A_{probe} versus B (b) for fields' intensities $I_{\text{probe}} = 20$ mW cm^{-2} and $I_{\text{sw}}^{\text{max}} = 100$ mW cm^{-2}. Results in (a) are for magnetic fields $B = 0$, 1 and 3 G and in (b) for standing-wave intensities $I_{\text{sw}} = 0$, 0.025, 0.5 and 1 $I_{\text{sw}}^{\text{max}}$.
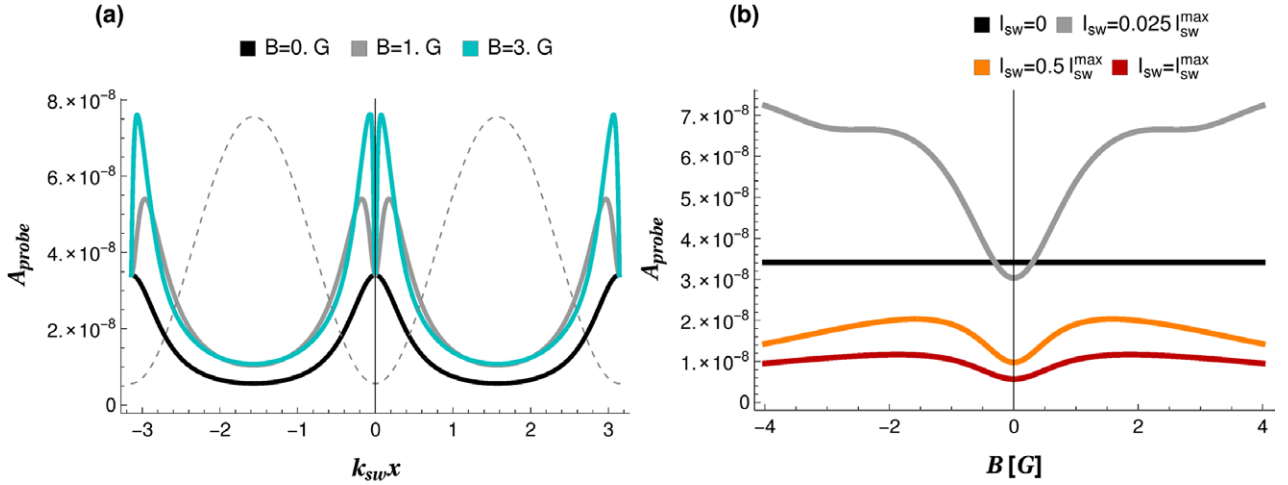
nearly constant probe absorption around the nodes for value $B = 1.8$ G in figure 5(a) and the formation of another narrow peak.

3.2. Configuration B

In configuration **B**, as presented in figure 1(b), the probe field is oriented along the magnetic field and the quantisation axis. Figure 6 shows the results for the FWHMs (a), base-contrast (b) and contrast (c) of the localisation pattern structures. The results for the structure widths show that the precision for atom localisation increases when intensity $I_{\text{sw}}^{\text{max}} \geqslant 10^{-2}$ mW cm^{-2}. The base-level of the localisation structures is low if either the field intensity is larger than 1 mW cm^{-2}. The results for the contrast suggest that the range $I_{\text{probe}} < 1$ mW cm^{-2} and $I_{\text{sw}}^{\text{max}} > 10^{-2}$ mW cm^{-2} induces a higher contrast of localisation structures. In short, the results in figure 6 show good localisation with high precision, low base-level and high contrast for small I_{probe} and large $I_{\text{sw}}^{\text{max}}$.

In figure 7(a) we present the localisation patterns for $I_{\text{probe}} = 10^{-4}$ mW cm^{-2} and $I_{\text{sw}}^{\text{max}} = 10$ mW cm^{-2} and for three values of the magnetic field $B = 0$, 1 and 2 G. The results show excellent atom localisation at the nodes of the standing-wave. At and around the anti-nodes positions' absorption is completely suppressed due to high standing-wave intensities exceeding the saturation intensity. The wide absorption maximum for $I_{\text{sw}} = 0$ in figure 7(b) corresponds to one-photon absorption since π-polarised light cannot induce EIT [41, 44]. The height of ther localisation peaks in figure 7(a) at the nodes decreases slightly with the increase in B due to the shifts of magnetic levels and lower absorption due to detuning from the resonance. The localisation peaks are broadened for small values of I_{sw} or near the nodes, where EIT is weaker for larger B (see figure 7(b)) resulting in a slight reduction in localisation efficiency.

Figure 8 shows the results when the probe field intensity is higher than the standing-wave intensities, i.e. for $I_{\text{probe}} = 20$ mW cm^{-2} and $I_{\text{sw}}^{\text{max}} = 1$ mW cm^{-2}. The results in figure 8(a)

show that for $B = 0$ the localisation pattern represents a sinusoidal curve with poor localisation precision. The results presented here and for similar intensities indicate that an increase in magnetic field can improve localisation due to a significant increase in the structure's contrast. At the nodes of the standing-wave, about 80% of the population is optically pumped to the edge levels, g_{-1} and g_{+1} by the π-polarised probe field's. The standing-wave field allows $\Delta m = \pm 1$ transitions too, which causes redistribution among the Zeeman sublevels and allows an increase in absorption at the positions between the nodes.

In figure 9 we present the results for a much stronger standing-wave field, $I_{\mathrm{probe}} = 20\,\mathrm{mW\,cm^{-2}}$ and $I_{\mathrm{sw}}^{\max} = 100\,\mathrm{mW\,cm^{-2}}$. As shown in figure 8(a), the peaks in the localisation pattern for $B = 0$ are very wide. The increase in magnetic field also leads to the formation of narrow dips at the nodes' position, but a much stronger standing-wave creates four localisation peaks near the nodes. Compared to the results in figure 8 probe absorption at the anti-nodes' positions is at a lower level (see figure 9(b)) due to a considerably stronger standing-wave field which exceeds saturation intensity. The result when the peak splits if the magnetic field is applied is similar to the results in figure 4(a), although the presence of a magnetic field here significantly improves localisation due to better detection precision and the increase in the peaks' contrast.

4. Conclusion

We studied the efficiency of 1D subwavelength atom localisation via the EIT phenomenon in a degenerate two-level system, by using two orthogonal optical fields and small magnetic fields. The localisation efficiency is analysed for two configurations, when the applied magnetic field is along the standing-wave or along the probe field polarisation. Two configurations enable different transitions between the Zeeman magnetic sublevels, the behaviour of the EIT and consequently the localisation patterns. The properties of the position-dependent probe absorption are studied for a large range of field intensities and different values of magnetic field. The range of intensities giving efficient subwavelength resolution localisation was obtained numerically by calculating the widths and contrasts of the narrow structures shown in the localisation patterns.

Our results show that both configurations can be used for obtaining narrow localisation structures with widths less than $0.5\%\,\lambda$. The results for configuration **A** reveal conditions where one can manipulate both the position and contrast of the localisation peaks by a small magnetic fields. If a strong standing-wave and weak probe field are applied, the results for configuration **B** show very efficient atom localisation for a large range of applied magnetic fields. The results for configuration **B** also indicate a range of optical field intensities when a magnetic field can be used to improve localisation. The behaviour of the position-dependent probe absorption is analysed through the mutual effects of the induced EIT, two optical fields of various strengths, below or above saturation, and the dependence on the applied magnetic field.

References

[1] Kapale K T 2013 *Progress in Optics* vol 58, ed E Wolf (Amsterdam: Elsevier) chapter 4, p 200
[2] Metcalf H and Van der straten P 1994 *Phys. Rep.* **244** 203
[3] Phillips W D 1998 *Rev. Mod. Phys.* **70** 721
[4] Collins G P 1996 *Phys. Today* **49** 18–21
[5] Wu Y and Cote R 2002 *Phys. Rev.* A **65** 053603
[6] Jin L, Sun H, Niu Y, Jin S and Gong S 2009 *J. Mod. Opt.* **56** 805
[7] Johnson K S, Thywissen J H, Dekker N H, Berggren K K, Chu A P, Younkin R and Prentiss M 1998 *Science* **280** 1583
[8] Boto A N, Kok P, Abrams D S, Braunstein S L, Williams C P and Dowling J P 2000 *Phys. Rev. Lett.* **85** 2733
[9] Evers J, Qamar S and Zubairy M S 2007 *Phys. Rev.* A **75** 053809
[10] Kapale K T, Qamar S and Zubairy M S 2003 *Phys. Rev.* A **67** 023805
[11] Quadt R, Collett M and Walls D F 1995 *Phys. Rev. Lett.* **74** 351
[12] Storey P, Collett M and Walls D 1992 *Phys. Rev. Lett.* **68** 472
[13] Kunze S, Rempe G and Wilkens M 1994 *Europhys. Lett.* **27** 115
[14] Brune M, Harlche M, Lefevere V, Maimond J M and Zagury N 1990 *Phys. Rev. Lett.* **65** 976
[15] Thomas J E and Wang L J 1995 *Phys. Rep.* **262** 311
[16] Rudy P, Ejnisman R and Bigelow N P 1997 *Phys. Rev. Lett.* **78** 4906
[17] Kunze S, Dieckmann K and Rempe G 1997 *Phys. Rev. Lett.* **78** 2038
[18] Kien F L, Rempe G, Schleich W P and Zubairy M S 1997 *Phys. Rev.* A **56** 2972
[19] Arimondo E 1996 *Progress in Optics* vol 35, ed E Wolf (Amsterdam: Elsevier) chapter 5, p 257
[20] Harris S E 1997 *Phys. Today* **50** 36
[21] Qamar S, Zhu S Y and Zubairy M S 2000 *Phys. Rev.* A **61** 063806
[22] Mompart J, Ahufinger V, Birkl G 2009 *Phys. Rev.* A **79** 053638
[23] Sahrai M, Tajalli H, Kapale K T and Zubairy M S 2005 *Phys. Rev.* A **72** 013820
[24] Ding C, Li J, Yang X, Zheng D and Xiong H 2011 *Phys. Rev.* A **84** 043840
[25] Paspalakis E, Terzis A F and Knight P L 2005 *J. Mod. Opt.* **52** 1685
[26] Liu C P, Gong S Q, Cheng D C, Fan X J and Xu Z Z 2006 *Phys. Rev.* A **73** 025801
[27] Cheng D C, Niu Y P and Gong S Q 2006 *J. Opt. Soc. Am.* B **23** 2180
[28] Ghafoor F, Qamar S and Zubairy M S 2002 *Phys. Rev.* A **65** 043819
[29] Xu J and Hu X M 2007 *Phys. Lett.* A **366** 276
[30] Wan R G, Kou J, Jiang L, Jiang Y and Gao J Y 2011 *J. Opt. Soc. Am.* B **28** 10
[31] Wang Z and Yu B 2014 *Laser Phys.* **24** 045203
[32] Qamar S, Mehmood A and Qamar S 2009 *Phys. Rev.* A **79** 033848
[33] Rahmatullah, Wahab A and Qamar S 2014 *Laser Phys. Lett.* **11** 045202
[34] Jendrzejewski F, Bernard A, Mller K, Cheinet P, Josse V, Piraud M, Pezz L, Sanchez-Palencia L, Aspect A and Bouyer P 2012 *Nat. Phys.* **8** 398

[35] Qi Y, Zhou F, Huang T, Niu Y and Gong S 2012 *J. Mod Opt.* **59** 1092

[36] Shen W B, Hu X M and Xu J 2008 *J. Phys. B: At. Mol. Opt. Phys.* **41** 185502

[37] Shui T, Wang Z, Cao Z and Yu B 2014 *Laser Phys.* **24** 055202

[38] Li H, Sautenkov V A, Kash M M, Sokolov A V, Welch G R, Rostovtsev Y V, Zubairy M S and Scully M O 2008 *Phys. Rev.* A **78** 013803

[39] Proite N A, Simmons Z J and Yavuz D D 2011 *Phys. Rev.* A **83** 041803

[40] Miles J A, Simmons Z J and Yavuz D D 2013 *Phys. Rev.* X **3** 031014

[41] Margalit L, Rosenbluh M and Wilson-Gordon A D 2013 *Phys. Rev.* A **87** 033808

[42] Meystre P and Sargent M III 1999 *Elements of Quantum Optics* 3rd edn (Berlin: Springer)

[43] Steck D A 2015 Rubidium 87 D Line Data, available online at http://steck.us/alkalidata (revision 2.1.5, 13 January 2015)

[44] Dimitrijević J, Krmpot A, Mijailović M, Arsenović D, Panić B, Grujić Z and Jelenković B M 2008 *Phys. Rev.* A **77** 013814